Data acquisition strategies to reduce cardiac-induced noise in brain maps of R_2* and magnetic susceptibility

Quentin Raynaud[1], Thomas Dardano[1], Rita Oliveira[1], Giulia Di Domenicantonio[1], Tobias Kober[2,3,4], Christopher W. Roy[2], Ruud B. van Heeswijk[2*], Antoine Lutti[1*]

[1]*Laboratory for Research in Neuroimaging, Department for Clinical Neuroscience, Lausanne University Hospital and University of Lausanne, Lausanne, Switzerland*

[2]*Department of Diagnostic and Interventional Radiology, Lausanne University Hospital and University of Lausanne, Lausanne, Switzerland.*

[3]*Advanced Clinical Imaging Technology, Siemens Healthineers International AG, Lausanne, Switzerland.*

[4]*LTS5, École Polytechnique Fédérale de Lausanne (EPFL), Lausanne, Switzerland.*

*Antoine Lutti and Ruud B. van Heeswijk contributed equally to this work.

Correspondence

Antoine Lutti

Laboratory for Research in Neuroimaging, Department for Clinical Neuroscience, Lausanne University Hospital, Ch. de Mont-Paisible 16, CH-1011 Lausanne

Email: antoine.lutti@chuv.ch

Abstract

Purpose

Cardiac pulsation increases the noise level in brain MR images. Maps of the transverse relaxation rate R_2* and magnetic susceptibility (QSM) are particularly affected by cardiac-induced noise as they are computed from gradient-echo data acquired at multiple echo times. Here, we introduce two data acquisition strategies to mitigate the impact of cardiac-induced noise in brain maps of R_2* and QSM.

Methods

The proposed strategies are based on the higher level of cardiac-induced noise near the k-space centre. Using a pseudo-spiral sampling trajectory, the first strategy allows for the acquisition of a specific number of averages at each k-space location, set from the local level of cardiac-induced noise. The second strategy synchronizes the acquisition with the cardiac cycle in real time. We compared in 10 healthy volunteers, the variability of data acquired across 4 repetitions and in the same session, using both strategies and with a standard linear trajectory.

Results

Compared to linear sampling, the pseudo-spiral trajectory reduced the variability of R_2* and QSM maps across repetitions by 26/28/22% and 19/18/16% in the brainstem/cerebellum/whole brain, for a 14% increase in scan time. The pseudo-spiral sampling also reduced the level of aliasing artifacts from pulsating blood vessels. The cardiac-triggered trajectory did not reduce the variability of R_2* or QSM maps.

Conclusion

Pseudo-spiral k-space trajectories can be designed to mitigate cardiac-induced noise in brain maps of the MRI parameters R_2* and QSM. Synchronization of the acquisition with the cardiac cycle in real time did not lead to any reduction in cardiac-induced noise.

Keywords:

Brain; cardiac-induced noise; Physiological noise; quantitative MRI; R2*; QSM; MRI relaxometry

1. Introduction

MRI relaxometry enables the non-invasive investigation of microscopic changes in brain tissue in patient populations.[1,2] Estimates of the transverse relaxation rate R_2* (=1/T_2*)[3] and magnetic susceptibility ('quantitative susceptibility mapping' - QSM)[4] are biomarkers of iron and myelin concentration within brain tissue,[5,6] and allow the investigation and may provide means for monitoring of the evolution of neurological diseases such as Parkinson's disease,[7,8] Alzheimer's disease,[9] and multiple sclerosis.[10]

Cardiac pulsation leads to a systolic blood pressure wave that travels to the brain and generates several types of periodic noise in brain MR images. Cardiac-induced noise can thus result from physiological effects such as head motion,[11] brain tissue deformation,[12,13] blood flow,[14–17] cerebrospinal fluid flow,[18,19] changes in the tissue's O_2/CO_2 concentration,[20,21] blood vessel pulsatile motion[22] and other effects.[23] It is most prominent in inferior and highly vascularized brain regions such as the orbitofrontal cortex,[19,24] brainstem,[25,26] cerebellum[27] and periventricular regions.[24,28] Cardiac-induced noise in MRI data results from the coupling between these underlying physiological processes and imaging parameters such as encoding gradients and echo times.[29,30] Changes of the B_0-field,[31] laminar flow[30,32] and motion[33,34] are coherent across an image voxel, which leads on the one hand to a net phase shift of the signal. Turbulent flow[35] and intra-voxel B_0 inhomogeneities[36] are incoherent across an image voxel and may on the other hand affect the magnitude of the signal.

In functional MRI, a series of image volumes are acquired at a rate of ~1Hz and the effect of cardiac pulsation on the time course of the data can be removed using dedicated models.[37–39] In MRI relaxometry, data acquisition strategies usually do not address cardiac-induced noise. Data acquisition requires several minutes and cardiac pulsation can lead to aliasing artifacts that are particularly prominent in lower brain regions such as the brainstem and cerebellum, as well as highly vascularized brain regions such as the temporal lobes. Cardiac-induced noise and the related aliasing artifacts are challenging to reduce with image-based post-processing techniques. Instead, tailored k-space sampling trajectories are generally preferred to ensure that this spatial aliasing remains incoherent.[40–42] It should be noted that these scrambling methods aim to mitigate the effect of cardiac-induced noise on structural MR images rather than reducing the amplitude of this noise in the acquired data. Other methods such as keyhole imaging or PROPELLER acquire the centre of k-space multiple times to resolve dynamic effects such as blood flow[43] or BOLD signals[44] and are tailored to increase SNR or reduce motion.[45,46] In non-brain imaging, dynamic keyhole acquisition can be used to resolve and mitigate breathing effects or motion.[47,48] The adaptation of these methods towards the reduction of cardiac-induced noise in structural brain images remains unexplored.

In this study, we introduce two data acquisition strategies that aim to reduce the level of cardiac-induced noise in brain relaxometry data.[49] These strategies are derived from a recent study of cardiac-induced noise in multi-echo data.[49] The first strategy, based on a Cartesian pseudo-spiral trajectory, allows for the acquisition of a specific number of averages at each k-space location, set according to the local level of cardiac-induced noise. The second strategy is inspired by existing cardiac-gating acquisitions used in diffusion[50,51] and functional MRI[52,53] and synchronizes the acquisition with cardiac pulsation to acquire the most sensitive data during the most stable part of the cardiac cycle. We evaluate the ability of both strategies to reduce the level of cardiac-induced noise in multi-echo data.

2. Methods

The proposed noise mitigation strategies are based on the abovementioned previous study that provided a full characterization of cardiac-induced noise in gradient-echo data.[49] Low-resolution 3D multi-echo data was acquired continuously for one hour in 5 participants. The participants' cardiac pulsation was recorded simultaneously. To resolve the effect of cardiac pulsation on R_2* maps, one hour worth of multi-echo data was reordered according to the phase of the cardiac cycle at the time of its acquisition, leading to 5D datasets with three spatial dimensions, one echo time dimension and a cardiac phase dimension. By analogy with other models of physiological noise,[37,39,54] cardiac-induced noise was modelled from Fourier series decomposition up to the second order of the change of the 5D data along its cardiac cycle dimension.[49] This allowed the estimation of the amplitude of cardiac-induced noise at each of k-space location and the identification of the most affected area of k-space, which was the centre.

Here, we first use the 5D models of cardiac-induced noise to conduct numerical simulations of candidate k-space sampling strategies and to evaluate their ability to reduce cardiac-induced noise in multi-echo data.

2.1. Strategy 1: Pseudo-spiral trajectory

The amplitude of the modelled cardiac-induced noise depends primarily on the radial distance to the centre of k-space along the two phase encoding directions (Figure 1A): 50-60% of cardiac-induced noise is located near the k-space centre ($|k| < 0.074$ mm^{-1}).[49] Based on this observation, we propose to acquire a number of averages at each k-space location that is derived from the local level of cardiac-induced noise, computed from the 5D datasets. This strategy allows for the reduction of the effective noise level at each k-space location:

$$N_{|k|,n} = var(S_{cardiac})/n, \tag{2}$$

where $N_{|k|,n}$ is the effective noise level in a ring of radius $|k|$ and n is the number of averages. $var(S_{cardiac})$ is the variance of the modelled cardiac-induced signal fluctuations, averaged across echoes. In peripheral areas of k-space ($|k| \geq 0.09$ mm^{-1}), where signal fluctuations arise primarily from thermal noise, one average is acquired: $n = 1$.

The averaging efficiency, i.e. the reduction in effective noise level from the acquisition of one additional average, can be expressed as:

$$E_{|k|,n} = N_{|k|,n+1} - N_{|k|,n} = N_{|k|,1}\left(\frac{1}{n+1} - \frac{1}{n}\right), \tag{3}$$

where $N_{|k|,1} = var(S_{cardiac})$ is the effective noise level when only one sample is acquired. Equation 3 shows that averaging efficiency decreases with an increasing number of averages (Figure 1B). Therefore, an effective noise level that is uniform across k-space leads to a prohibitive increase in acquisition time. Instead, to preserve the efficiency of the averaging, the number of averages is determined at each k-space location by ensuring that the net reduction in noise level is at least equal to that of a data point in an area dominated by thermal noise, if another average were to be acquired there:

$$E_{|k|<0.09,n} = N_{|k|,1}\left(\frac{1}{n+1} - \frac{1}{n}\right) \geq -\frac{1}{2} N_{|k|\geq 0.09,n=1} \tag{4}$$

Figure 1C shows the target number of samples across k-space. To achieve this k-space sampling distribution while minimizing eddy currents, a pseudo-spiral Cartesian sampling trajectory[55] was implemented with arms located within the 2D plane of the phase-encoding, allowing data acquisition during the inwards and outward traversal of k-space.[56,57] Trajectories with different number of points per arms, number of arms, arms curvatures and sampling density variations were simulated. The pseudo-spiral trajectory that led to the closest match with the target number of samples consisted of 120 spiral arms with 100 points each (Figure 1D). The corner k-space frequencies not acquired with the pseudo-spiral trajectory were acquired using a linear scheme at the end of the acquisition (i.e., black regions of k-space in Figure 1D).

2.2. Strategy 2: Cardiac-triggered sampling

The first quarter of the cardiac cycle after the detection of the peak of the pulse wave at the finger exhibits a lower level of cardiac-induced signal instabilities (Figure 2A). From this observation, we derived a sampling strategy that synchronizes the acquisition with the cardiac cycle. Note that instead of cardiac gating techniques that prevent data acquisition over a fraction of the cardiac-cycle, this strategy locks data acquisition to the cardiac phase by pausing at specific k-space locations.

This strategy starts like a standard linear trajectory at one corner of k-space: for each k-space line along the slow phase-encoding direction, data is acquired linearly along the fast-encoding direction, at a rate of 1/TR = 25Hz (Figure 2B). As a result, the phase of the cardiac cycle at the time of acquisition of the data varies smoothly along the fast phase-encode direction. However, data acquisition is locked to the cardiac cycle by means of two cardiac-triggered k-space lines aligned along the slow-encoding direction (Figure 2B). Upon reaching these lines, data acquisition is paused, maintaining RF excitation to preserve the steady state of the MRI signal. K-space sampling is resumed when the next peak of the pulse wave is detected. As a result, acquisition of the subsequent data points takes place during the most stable period of the cardiac cycle (i.e. the first quarter after systole). Note that to limit the increase of scan time due to this triggering strategy, the triggering only occurs for $|k| < 0.125\text{mm}^{-1}$, which contains most of the cardiac-induced noise.[49]

To identify the position of the cardiac-triggered lines that leads to maximal reduction of cardiac-induced noise, we performed numerical simulations of data acquisition using the 5D model of cardiac-induced noise, using simulated cardiac-cycles with a wide range of heart rates and the parameter settings of in-vivo acquisitions (repetition time (TR): 40ms; k-space size: 88 along the fast-encoding direction). As a measure of signal instability due to cardiac pulsation, we computed from the 5D data, at each k-space location in the phase-encode plane, the time derivative of the modelled cardiac-induced noise at the time of acquisition of the data. The local time-derivative estimates were summed across k-space to produce a global estimate of signal instability due to cardiac pulsation and averaged across echoes and participants.

The numerical simulations were conducted for every possible position of the two cardiac-triggering lines and for cardiac periods ranging from 600ms to 1000ms in steps of 10ms. The optimal position of the cardiac-triggering lines, identified as leading to minimal global signal instability due to cardiac pulsation, was $k = -0.0625$ mm^{-1} and $k = -0.0057$ mm^{-1} (k-space index 34 and 44 over 88) along the fast-encoding direction (Figure 2C). As expected, the optimal triggering lines are located near the centre of k-space, which contains most of the cardiac-induced noise. This strategy has the additional advantage of leading to an effective locking of the phase of the cardiac cycle during the acquisition of the sensitive data, enforcing smooth phase change along the slow phase-encode direction and constraining spatial aliasing of cardiac-induced noise in image space.[58]

2.3. MRI data acquisition and analyses

To assess the reduction in cardiac-induced noise from the two proposed strategies, data was acquired in 10 participants (7 females, 27±7 years old), with a 3T MRI scanner (Magnetom Prisma, Siemens Healthineers, Forchheim, Germany) and a 64-channel head-neck coil. The participants' cardiac pulsation was recorded using a pulse-oximeter attached to their finger. To ensure optimal quality of the pulse-oximeter signal, participants were offered a blanket and a hot water bottle was placed near their hand. The study was approved by the local ethics committee and all participants gave their written informed consent prior to participation.

2.3.1. MRI protocol

MRI data was acquired with a custom-made 3D multi-echo FLASH sequence capable of k-space sampling with a standard linear Cartesian trajectory as well as the proposed pseudo-spiral trajectory and cardiac triggering. 15 echo images were acquired after radiofrequency (RF) excitation with echo times TE=2.34ms to 35.10ms. The repetition time was 40ms, the RF excitation flip angle was 16° and image resolution was 2x2x2mm^3. GRAPPA[59] was used with acceleration factor of 2 and 24 reference lines. The scan time was 4:31 minutes for the standard linear sampling, 5:09 minutes (+14%) for the pseudo-spiral sampling and 5:22 minutes (+19±1%) for the cardiac-triggered sampling. Four scans were conducted for each sampling strategy to quantify the reproducibility of the data across repetitions. The resolution of the data was low to keep the total scan time reasonable. Additional MRI data was acquired on a single participant (male, 30 years old) with a higher image resolution of 1.2x1.2x1.2mm^3, representative of relaxometry protocols used in neuroscience studies.[60–62] The other acquisition parameters were unchanged. Three repetitions of the high-resolution protocol were conducted with standard linear sampling (scan time 10:28 minutes) and pseudo-spiral sampling (scan time 13:30 minutes (+29%)).

All acquisition protocols also included an MP-RAGE[63] image for segmentation and anatomical reference (1mm^3 resolution, TR/TE = 2000/2.39ms, GRAPPA[59] acceleration factor 2 with 24 reference lines, RF excitation angle = 9°, acquisition time 4:16 minutes). Two 3D FLASH datasets were acquired with the head- and body coils for signal reception (4×4×4mm^3 image resolution, TR/TE=5.72ms/2.34ms, excitation flip angle=6°, acquisition time 16s) and used subsequently for the computation of the coil sensitivity maps.[64]

2.3.2. Image reconstruction

Brain images were reconstructed offline using Matlab (version 2022a, The MathWorks, Natick, MA). Coil sensitivity maps were computed as the ratio of the (4mm)^3 resolution data acquired with the head and body coils.[64,65] For the pseudo-spiral sampling, the multiple samples acquired at each k-space location were averaged. Coil-specific images were reconstructed with GRAPPA[59] (https://github.com/mchiew/grappa-tools) and combined by performing a SENSE[65] reconstruction with an acceleration factor of 1.

2.4. Computation and analysis of the qMRI maps

2.4.1. Relaxometry and QSM

R_2* maps were computed voxel-wise from multi-echo images using a regression of the log signal with the corresponding echo times.[66] The noise level on the R_2* estimates was calculated as the root-mean-squared error (RMSE) between the MR signal and the R_2* fit.

Maps of magnetic susceptibility (QSM) were generated from the phase of the MR data using bespoke scripts adapted from https://github.com/fil-physics/MPM_QSM and following the ISMRM consensus guidelines.[67] The phase maps were unwrapped using ROMEO[68] with an additional correction for linear

phase offsets induced by bipolar readouts.[69] Brain masks were generated with BET from FSL[70] and underwent subsequent refinement through multiplication with a phase-quality-based mask obtained during the ROMEO unwrapping process, and any holes present within the resulting mask were subsequently filled. Removal of the background field was conducted with the Projection onto Dipole Fields algorithm[71] available in the SEPIA toolbox.[72] Finally, dipole inversion was computed using the STAR-QSM algorithm[73] provided in the SEPIA toolbox, using the entire brain as a reference. In one subject, an interhemispheric calcification was manually masked out and dipole inversion was conducted using this adjusted mask.

2.4.2. Image segmentation and statistical analysis

Image coregistration and segmentation were conducted using Statistical Parametric Mapping (SPM12, Wellcome Centre for Human Neuroimaging, London, UK). The MP-RAGE images were segmented into maps of grey and white matter probabilities using Unified Segmentation.[74] Whole-brain masks were computed from the grey and white matter segments and included voxels with a combined probability of 0.9 or above. As described in Lutti et al.,[60] regional masks were computed from the grey matter maximum probability labels computed in the 'MICCAI 2012 Grand Challenge and Workshop on Multi-Atlas Labeling' (https://masi.vuse.vanderbilt.edu/workshop2012/index.php/Challenge_Details), using MRI scans from the OASIS project (http://www.oasis-brains.org/) and labelled data provided by Neuromorphometrics, Inc. (http://neuromorphometrics.com/) under academic subscription.

To compare the two proposed sampling trajectories with the standard linear trajectory, we computed the variability of R_2*, RMSE, and QSM across repetitions and the mean RMSE. This is because cardiac-induced noise induces fluctuations across the cardiac cycle of both R_2* and RMSE estimates.[49] The fluctuations of R_2* reflect exponential-like effects of cardiac pulsation on signal intensities, with an amplitude that increases with the echo time. The fluctuations of RMSE reflect effects of cardiac pulsation that cannot be attributed to a change in R_2*. As a result of these fluctuations, in standard gradient-echo acquisitions, the estimates of R_2* and RMSE depend on the time of acquisition of the data relative to the cardiac cycle. For data acquisition schemes that are not synchronized with the cardiac cycle, the fluctuations of R_2* and RMSE across the cardiac cycle lead to increased variability of R_2* and RMSE across repetitions as well as an increase in the mean RMSE. Although the effect of cardiac pulsation on the phase of the MRI signal was not investigated in our previous work, we expect a similar effect of cardiac pulsation on the variability of QSM estimates across repetitions. We therefore computed the variability of the parameters R_2*, RMSE, and QSM across repetitions and the mean RMSE to assess the level of cardiac-induced noise in multi-echo data acquired using a standard cartesian linear trajectory and the proposed pseudo-spiral and cardiac-triggered trajectories. Statistical comparisons of cardiac-induced noise between trajectories were conducted in the brainstem and cerebellum – inferior brain regions that exhibit large cardiac-induced effects, and in the whole-brain. The significance of the differences in the variability of R_2*, RMSE and QSM as well as the mean RMSE between trajectories was calculated using two-sided Student's t-tests of the standard deviation of the parameter estimates across repetitions, averaged within each region of interest.

These statistical analyses were also conducted on the mean R_2* estimates across repetitions obtained from the three sampling trajectories. Because the standard linear and pseudo-spiral trajectories are not synchronized with cardiac pulsation, the mean parameter estimates between repetitions are a measure of the true mean values across the cardiac cycle. As a result, no systematic differences in the mean parameter estimates were expected between the standard linear and pseudo-spiral trajectories. However, the cardiac-triggered trajectory enforces acquisition of the most sensitive k-space data during the 1st quarter of the cardiac cycle (Figure 2B). Therefore, the mean parameter estimates between repetitions are not a measure of the mean parameter values across the cardiac cycle and systematic differences with the linear and pseudo-spiral trajectories may arise. Calculation of QSM

estimates requires subtracting the value of all voxels by a reference value taken across the whole brain and CSF.[75] Therefore, we the mean QSM values is similar by construction between each sampling.

3. Results

In the 10 healthy volunteers, when considering all brain voxels, the mean R_2* values across repetitions of the pseudo-spiral trajectory and cardiac-triggered acquisitions deviate from those of the standard linear trajectory by -0.15s^{-1} and -0.07s^{-1} respectively. These systematic differences in R_2* between acquisition strategies are less than one percent of typical R_2* values in the brain parenchyma (R_2* ~ 20s^{-1}). With the pseudo-spiral trajectory, the variability of R_2* across repetitions is reduced by 26/28/22% in the brainstem/cerebellum/whole-brain compared to the standard linear trajectory (Table 1 and Figure 3, p≤0.017). This is much larger than the $\sqrt{1.14} \sim 6.7\%$ reduction in variability due to the 14% additional samples of the pseudo-spiral trajectory, which would be expected when thermal noise dominates signal variance. With cardiac triggering, the variability of R_2* across repetitions is reduced by 6/6/3% in the brainstem/cerebellum/whole-brain respectively, for an increase in scan time of ~19% (Figure 3, p≥0.52). This is less than the reduction in variability expected from data acquired with the standard linear trajectory with 19% more samples to improve SNR ($\sqrt{1.19} \sim 9.0\%$). Post-hoc analyses were conducted to verify that the underwhelming reproducibility of the data acquired with cardiac triggering is not due to a faulty synchronization of data acquisition with the participants' cardiac cycle (see Supplementary Material S1).

Compared to standard linear sampling, the mean RMSE is lower by 5/3/2% with the pseudo-spiral trajectory (p≥0.06) and higher by 1/2/1% with cardiac triggering (p≥0.33), in the brainstem/cerebellum/whole-brain respectively (see Table 1 and Figure 4B). With the pseudo-spiral trajectory, the variability of RMSE across repetitions is lower by 17/17/13% in the brainstem/cerebellum/whole-brain compared to standard linear sampling (Figure 4, p≤0.046). With cardiac triggering, the variability of RMSE across repetitions is higher by 5/1/0% (Figure 4, p≥0.58).

As expected, the mean QSM value across repetition is the same for all three sampling strategies. With the pseudo-spiral trajectory, the variability of the QSM estimates across repetitions is lower than that of the standard linear trajectory by 19/18/16% in the brainstem/cerebellum/whole-brain (Figure 5, p≤0.015). With the cardiac triggering, the variability of the QSM estimates across repetitions is lower by 4/5/4% (Figure 5, p≥0.38).

The high-resolution data acquired with the standard linear trajectory shows a clear pattern of increased variability across repetitions in inferior brain regions (Figure 6A). In particular, maps of R_2* variability show aliasing along the anterior-posterior direction of cardiac-induced noise originally located e.g., in the Circle of Willis. This aliasing is not present in the data acquired with the pseudo-spiral trajectory. The variability of the R_2* estimates across repetitions is lower by 31/36/36% in the brainstem/cerebellum/whole-brain with the pseudo-spiral trajectory than the standard linear trajectory. The variability of the QSM estimates is lower by 27/26/32% with the pseudo-spiral trajectory than the standard linear trajectory in the brainstem/cerebellum/whole-brain (Figure 6B). The reduction in R_2* and QSM variability is larger than the $\sqrt{1.29} \sim 13.6\%$ reduction due to the 29% of additional samples of the pseudo-spiral trajectory, which would be expected when thermal noise dominates signal variance. R_2* maps computed from data acquired with the standard linear trajectory also show aliasing of cardiac-induced noise along the anterior-posterior direction (Figure 6C). With the

pseudo-spiral trajectory, this aliasing is not present, and the delineation of the white-grey matter is improved. The QSM data acquired with linear sampling show large streaking artifacts[73] around the Circle of Willis that are strongly reduced with the pseudo-spiral trajectory (Figure 6D).

4. Discussion

In this work, we proposed two new sampling strategies to reduce the level of cardiac-induced noise in brain maps of R_2* and magnetic susceptibility. These strategies were derived from a recent characterization of cardiac-induced noise in brain multi-echo data.[49] The first sampling strategy acquires a specific number of averages at each k-space location that was determined from the local level of cardiac-induced noise to maintain a uniform effective noise level across k-space. The second sampling strategy synchronizes data acquisition with the cardiac cycle of the participant to acquire the most sensitive region of k-space in the part of the cardiac cycle where MRI signal is most stable. Both sampling strategies primarily target the k-space centre, which contains most of the cardiac-induced noise. The ability of both proposed sampling strategies to reduce cardiac-induced noise was assessed from estimates of the transverse relaxation rate (R_2*), fitting residuals (RMSE) and magnetic susceptibility (QSM) computed from the multi-echo data.

In inferior brain regions, changes of up to $3s^{-1}$ in R_2* take place across the cardiac cycle.[49] With acquisition strategies not synchronized with cardiac pulsation, the timing of data acquisition within the cardiac period varies across repetitions, enhancing the variability of the R_2* and QSM estimates. With the standard linear trajectory, the ROI-averaged variability of R_2* maps was $1.8\text{-}2.3s^{-1}$ across repetitions, higher than the ROI-averaged variability of R_2* across the cardiac cycle in the original characterization of cardiac-induced noise ($0.8\text{-}1.4s^{-1}$).[49] This is likely due to the difference in SNR resulting from the higher resolution used in this work ($2x2x2mm^3$ instead of $2x4x4mm^3$). Additionally, the current data displays a substantial amount of spatial aliasing along the slow phase-encode direction (anterior-posterior in Figure 3A), leading to increased variability away from the source of cardiac-induced noise. This aliasing was not present in the original characterization of cardiac-induced noise because the k-space data was binned according to its cardiac phase before image reconstruction.

The pseudo-spiral trajectory rendered the maps of the variability of the R_2*, QSM and RMSE parameters more spatially uniform. The variability of R_2* across repetitions was reduced by 26/28/22% compared to standard linear sampling in the brainstem/cerebellum/whole-brain, lower than the fraction of the variability in R_2* across the cardiac cycle in the original study (~35%).[49] Similarly, the variability of RMSE across repetitions was reduced by 17/17/13%, lower than the variability across the cardiac cycle in the original study (~29%).[49] These findings are consistent with the lower impact of physiological noise in the high-resolution data presented here, although the pseudo-spiral trajectory may have allowed for the correction of other types of physiological noise such as respiration.[76] Similar improvements in reproducibility with the pseudo-spiral trajectory were found with the QSM estimates (~15-20%).

The standard linear and pseudo-spiral strategies are not synchronized with the cardiac cycle and are expected to yield mean values across repetitions close to the mean across the cardiac cycle. This is particularly true for the pseudo-spiral strategy, which acquires multiple averages near the k-space centre. The mean R_2*, QSM and RMSE values showed minimal differences between standard linear and pseudo-spiral trajectories, in agreement with expectations. However, cardiac triggering enforces

the acquisition of data within a narrow period of the cardiac cycle and might be expected to yield different R_2*, QSM and RMSE values. This was not observed here.

One limitation of pseudo-spiral trajectories is that they can induce stronger eddy current artefacts than their linear counterparts, due to the faster traversing in k-space along the two-phase encoding directions.[77–81] Eddy currents can be mitigated by reducing the amplitude or slew rate of the encoding gradients, increasing the TR, or acquiring more points on each spiral arm to reduce the k-space distance between consecutive points. Moreover, scanner heating leads to a drift of the main magnetic field that can degrade the quality of data acquired with pseudo-spiral trajectories. This effect can be corrected using phase navigator data acquired throughout the scans.[82] Preliminary phantom acquisitions were performed to ensure identical image quality and artifact-free images with both the standard linear and pseudo-spiral trajectories (not shown). A useful but potentially risky feature of this type of sampling is that it renders cardiac-induced noise, as well as other types of physiological noise, incoherent.[41] With pseudo-spiral trajectories, cardiac-induced noise does not remain localized at its source but spreads across the 2D plane of the phase-encode directions. Numerous methods exist to filter out incoherent aliasing artifacts, creating an opportunity for further data quality improvement or higher acceleration factors.[83–85] In this study, cardiac-induced aliasing artifacts were of low amplitude due to the large numbers of averages near the centre of k-space, where most cardiac-induced noise is located. It should also be noted that, while the cardiac-triggering strategy is an active noise reduction approach that specifically targets cardiac-induced noise, the pseudo-spiral trajectory is a passive approach based on the acquisition of multiple averages. Therefore, the pseudo-spiral trajectory does not target specifically cardiac-induced noise and acts on other sources of physiological noise such as motion and breathing.

Cardiac triggering was not effective at reducing the variability of R_2*, QSM and RMSE estimates across repetitions. Care was put into getting high-quality pulse oximeter signals and all post-hoc analyses indicate that cardiac triggering performed as expected. The number of cardiac-triggering lines was set to 2, deemed sufficient to have a reliable and efficient synchronization (Figure 2). More cardiac-triggering lines could have led to a better synchronization, at the cost of a longer scan time. Also, pulse oximeters might be too unreliable to accurately measure the phase of the cardiac cycle, resulting in a bad synchronization between the acquisition and the real cardiac phase.[87] Moreover, even under the assumption that the synchronization was ideal, the initial assumption that cardiac-induced noise is consistent across heartbeats might not always hold: changes in cardiac-induced noise between heartbeats may lead to signal instabilities sufficient to counteract the intended benefits of cardiac triggering. Also, suspension of data acquisition may lead to discontinuities of the head position between data points acquired consecutively, resulting in enhancing aliasing.[79]

5. Conclusion

In this work, we evaluated two candidate strategies to reduce the level of cardiac-induced noise in brain maps R_2* and magnetic susceptibility (QSM). Both sampling strategies were motivated from a previous characterization of cardiac-induced noise in brain multi-echo data.[49] The first sampling strategy relies on a Cartesian pseudo-spiral trajectory to acquire several averages at k-space locations that depend on the local level of cardiac-induced noise. The second strategy synchronizes data acquisition with cardiac pulsation in real time to acquire the most sensitive area of k-space during the least noisy part of the cardiac cycle ('cardiac triggering').

Compared to standard linear sampling, cardiac triggering did not efficiently reduce the variability of R_2* and QSM estimates across repetitions. Conversely, the pseudo-spiral sampling reduced the variability of R_2* and QSM estimates across repetitions by 15-30%, for an increase in scan time of 14%. The largest improvements in variability were observed in inferior brain regions such as the brainstem and cerebellum. This strategy further improves the reproducibility of R_2* and QSM estimates by reducing the aliasing of cardiac-induced noise across the field of view, away from its original location.[82–86]

Data availability statement

One of the 5D datasets used for the optimization of the sampling strategies can be found here (DOI:10.5281/zenodo.7428605). The high-resolution dataset is available online here (DOI:10.5281/zenodo.12685105).

Funding information

This work was supported by the Swiss National Science Foundation (grant no 320030_184784 to AL; 32003B_182615 and CRSII5_202276 to RBvH) and the Fondation ROGER DE SPOELBERCH.

Ethics approval statement

This study received approval from the local ethics committee and all participants gave their written informed consent prior to participation.

6. Figures

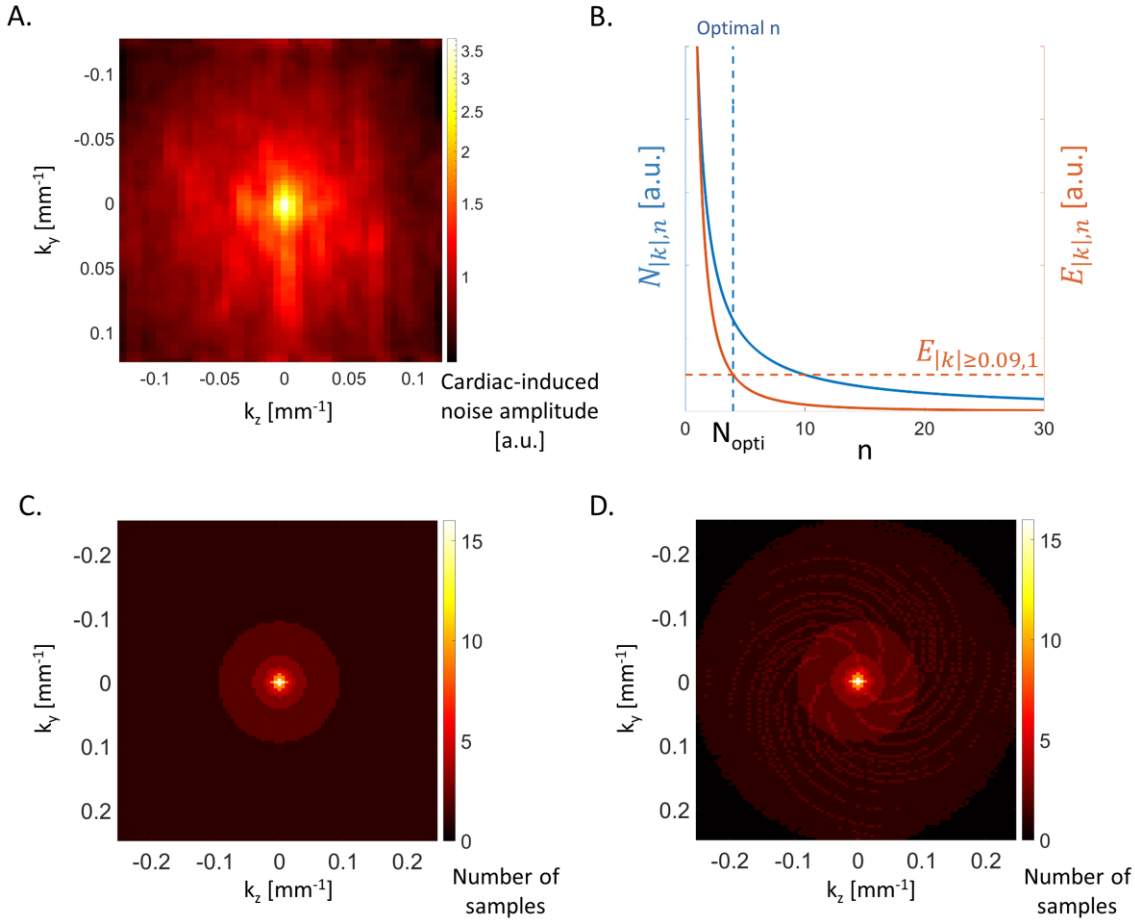

Figure 1: Pseudo-spiral trajectory for the reduction of cardiac-induced noise. (A) Distribution of cardiac-induced noise in k-space obtained from the 5D dataset. (B) Effective noise level ($N_{|k|,n}$) and averaging efficiency ($E_{|k|,n}$) as a function of the number of samples *n*. The effective noise level depends on the inverse of the number of samples *n*. The optimal number of samples N_{opti} is reached when the averaging efficiency ($E_{|k|,n}$) equals that of a point dominated by thermal noise. (C) Target k-space distribution of the optimal number of samples, resulting in 14% more samples than a standard linear trajectory. (D) Number of samples achieved with the optimal pseudo-spiral trajectory. The k-space edges (in black) are acquired linearly at the end of the pseudo-spiral acquisition.

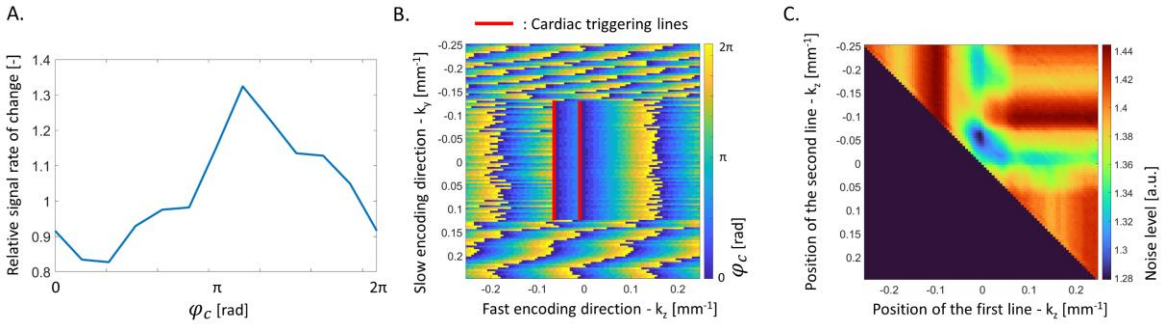

Figure 2: Cardiac-triggered sampling for the reduction of cardiac-induced noise. (A) Relative mean signal rate of change across the cardiac cycle obtained from the 5D dataset. The cardiac cycle was recorded from a finger pulse-oximeter. The first quarter of the cardiac cycle ($0 < \varphi_c < \frac{\pi}{2}$) exhibits a lower level of cardiac-induced signal change. (B) Proposed linear k-space trajectory with cardiac triggering that starts in the top left. The triggering enforces the acquisition of the k-space centre data, which is the most sensitive to cardiac-induced noise, during this period. As a result, the changes in the phase of the cardiac cycle at the time of acquisition of the data are smooth. The red lines indicate the k-space frequencies at which cardiac triggering is performed. (C) Cardiac-induced noise level based on the position of two cardiac-triggering lines for an acquisition with a k-space size of 128x88 and a TR of 40ms. The minimal cardiac-induced noise amplitude was found when the two lines are positioned at $k = -0.0625$ mm^{-1} and $k = -0.0057$ mm^{-1}.

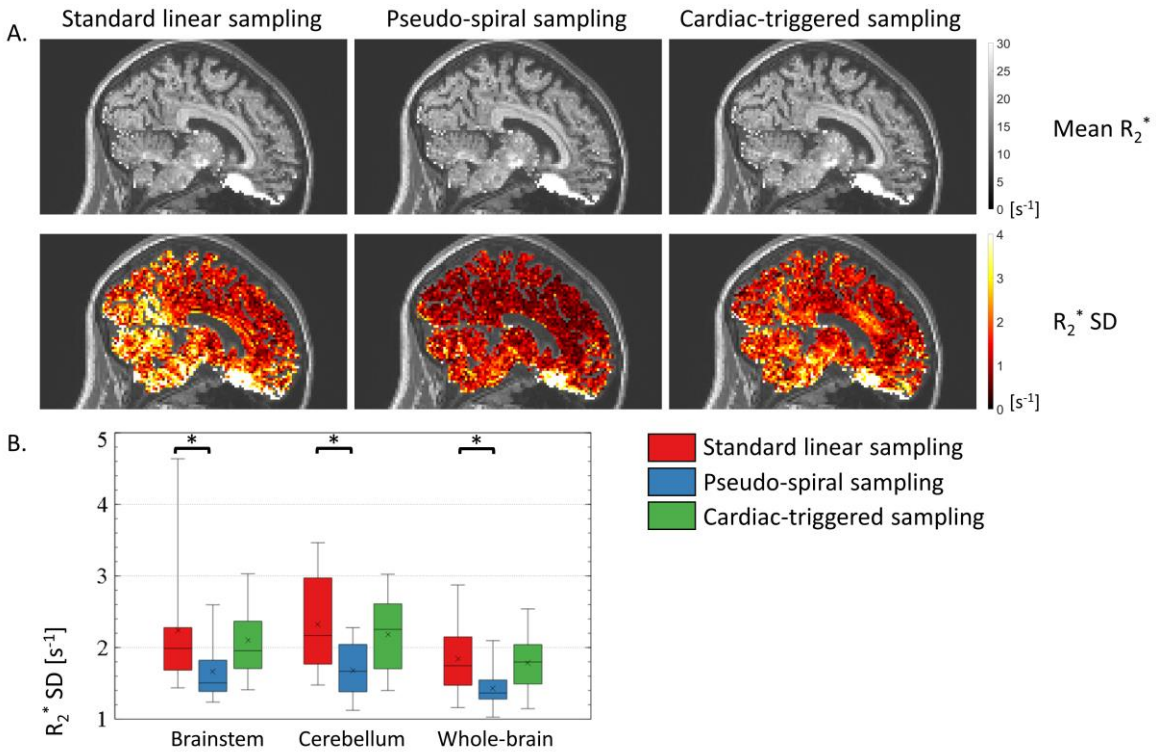

Figure 3: (A) Mean and standard deviation (SD) across repetitions of R_2* maps computed from data acquired with the standard linear and pseudo-spiral trajectories and with cardiac triggering, for a single volunteer. (B) SD of R_2* in the brainstem, cerebellum and whole-brain averaged over the 10 healthy volunteers. The pseudo-spiral trajectory reduces the SD of R_2* across repetitions by 26, 28 and 22% respectively ($p \leq 0.017$) compared to standard linear sampling. For cardiac-triggered sampling this reduction is of 6, 6 and 3% only ($p \geq 0.52$).

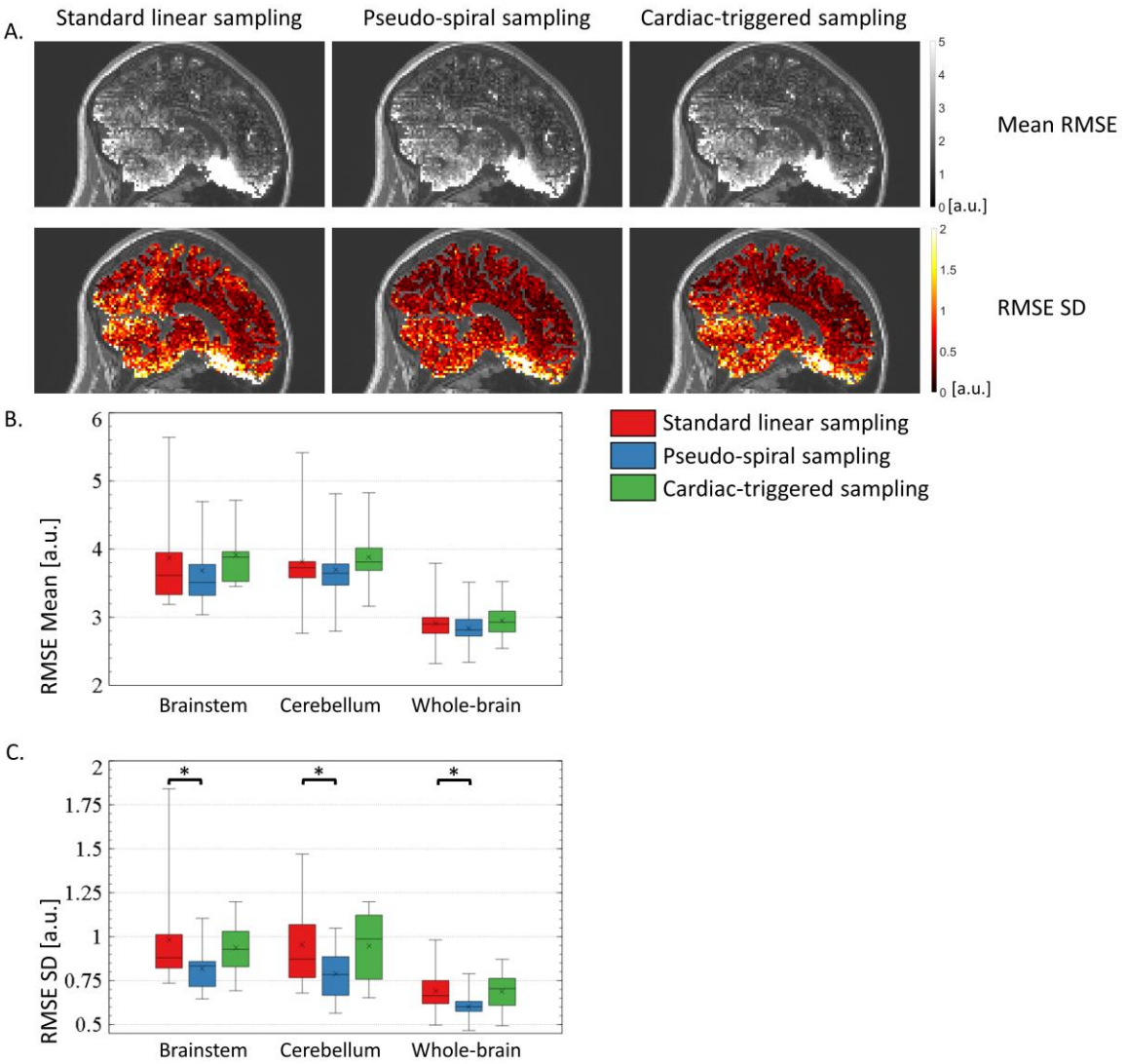

Figure 4: (A) Mean and standard deviation (SD) across repetitions of R_2* fitting residual estimates (root mean square error - RMSE) computed from data acquired with the standard linear and Cartesian pseudo-spiral trajectories, and with cardiac triggering. (B) Mean RMSE in the brainstem, cerebellum and whole-brain. The pseudo-spiral trajectory reduces the mean RMSE by 5, 3 and 2% compared to the standard linear trajectory ($p \geq 0.12$). For the cardiac-triggered sampling this reduction is of 1, 2 and 1% ($p \geq 0.33$). (C) SD of RMSE in the brainstem, cerebellum and whole-brain. The pseudo-spiral trajectory reduces the SD of RMSE by 17, 17 and 13% compared to the standard linear trajectory ($p \leq 0.046$). For the cardiac-triggered sampling this reduction is of 5, 1 and 0% only ($p \geq 0.58$).

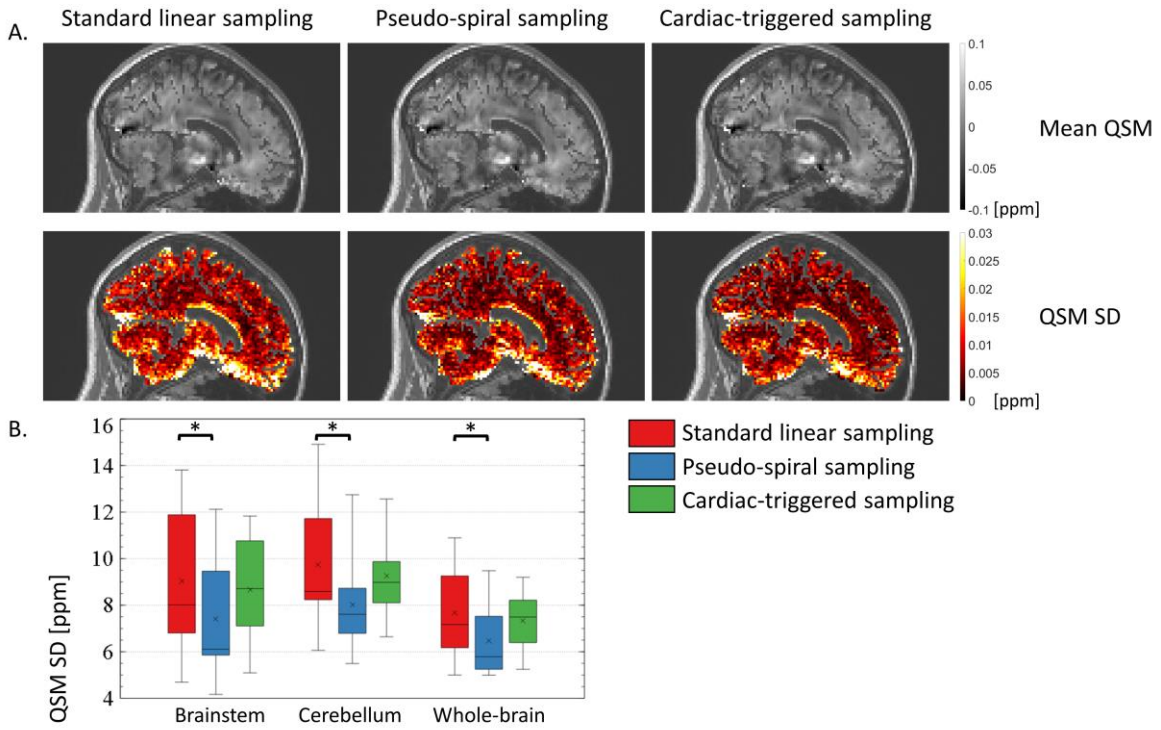

Figure 5: (A) Mean and standard deviation (SD) across repetitions of QSM estimates computed from data acquired with the standard linear and pseudo-spiral trajectories, and with cardiac triggering. (B) SD of QSM in the brainstem, cerebellum and whole brain. The pseudo-spiral trajectory reduces the SD of QSM by 19, 18 and 16% compared to standard linear sampling ($p \leq 0.015$). For the cardiac-triggered sampling this reduction is of 4, 5 and 4% ($p \geq 0.38$).

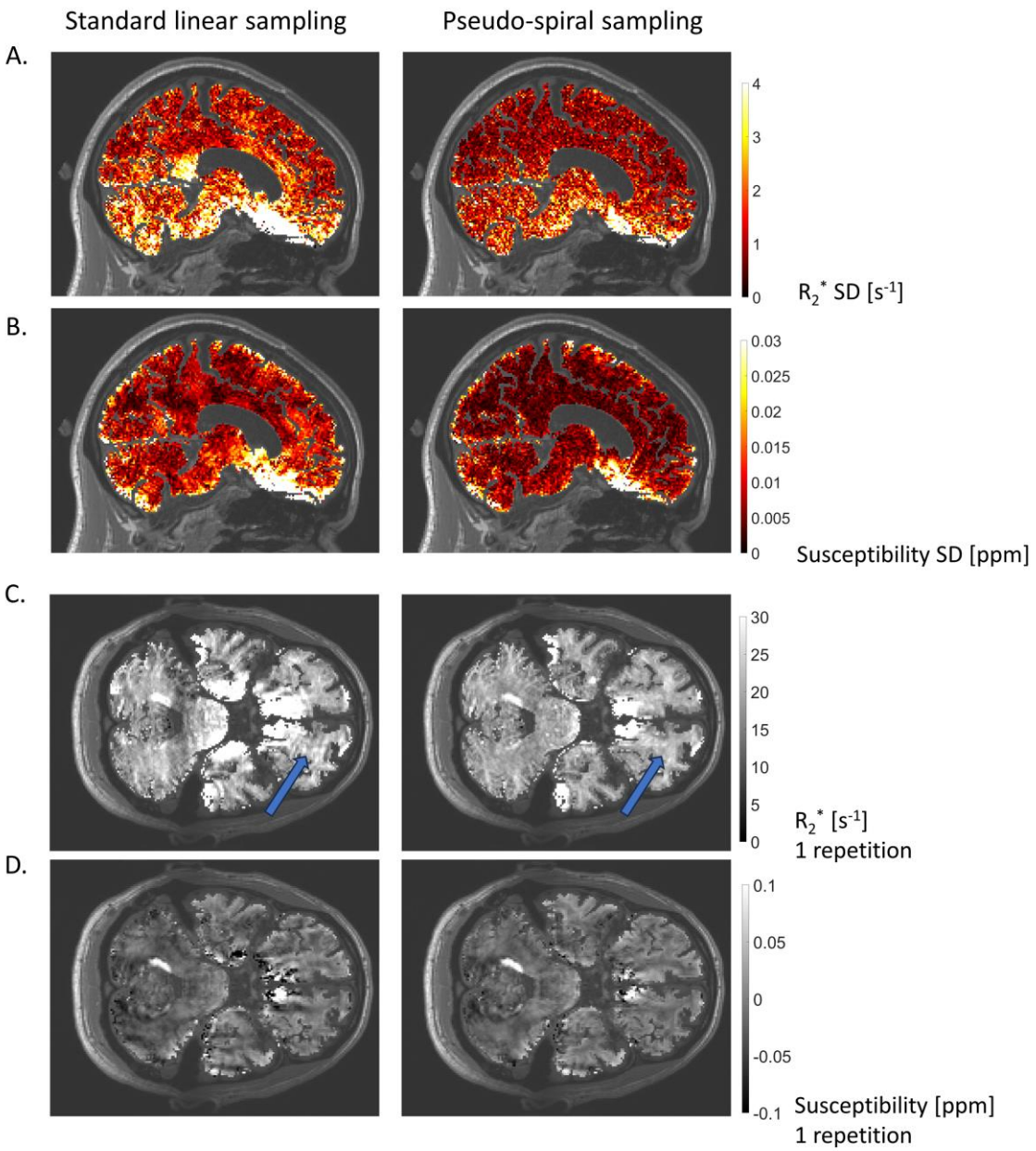

Figure 6: Maps of R_2* and QSM computed from higher resolution data acquired with standard linear and Cartesian pseudo-spiral trajectories. (A) R_2* standard deviation (SD) across repetitions. (B) QSM SD across repetitions. (C) R_2*estimates for one repetition. (D) QSM estimates for one repetition. Lower SDs can be observed throughout the brain for the Cartesian pseudo-spiral sampling. In the standard linear sampling maps, coherent aliasing (arrows) can be observed along the anterior-posterior direction, which is absent in the Cartesian pseudo-spiral maps.

7. Tables

	Sampling	Brainstem	Cerebellum	Whole brain
R_2^* SD [s^{-1}]	Standard linear	2.24±0.93	2.33±0.73	1.84±0.52
	Pseudo-spiral	1.67±0.43	1.68±0.41	1.43±0.32
	Cardiac triggering	2.10±0.55	2.18±0.56	1.79±0.43
RMSE mean [a.u.]	Standard linear	3.87±0.78	3.81±0.71	2.90±0.39
	Pseudo-spiral	3.69±0.58	3.70±0.54	2.84±0.33
	Cardiac triggering	3.92±0.46	3.88±0.53	2.95±0.28
RMSE SD [a.u.]	Standard linear	0.98±0.32	0.95±0.26	0.69±0.14
	Pseudo-spiral	0.82±0.13	0.79±0.15	0.60±0.09
	Cardiac triggering	0.94±0.16	0.95±0.21	0.69±0.12
QSM SD [ppm] $x10^3$	Standard linear	9.03±3.27	9.74±2.79	7.66±2.01
	Pseudo-spiral	7.41±2.68	8.02±2.10	6.50±1.56
	Cardiac triggering	8.66±2.41	9.26±1.76	7.33±1.30

Table1: Regional averages of the variability of the R_2*/RMSE/QSM and mean RMSE estimates across repetitions, computed from data acquired with the standard linear and pseudo-spiral trajectories and with cardiac triggering.

8. References

1. Tabelow K, Balteau E, Ashburner J, et al. hMRI – A toolbox for quantitative MRI in neuroscience and clinical research. *NeuroImage*. 2019;194:191-210. doi:10.1016/j.neuroimage.2019.01.029

2. Weiskopf N, Edwards LJ, Helms G, Mohammadi S, Kirilina E. Quantitative magnetic resonance imaging of brain anatomy and in vivo histology. *Nature Reviews Physics*. 2021;3(8):570-588. doi:10.1038/s42254-021-00326-1

3. Cohen-Adad J. What can we learn from T2* maps of the cortex? *NeuroImage*. 2014;93:189-200. doi:10.1016/j.neuroimage.2013.01.023

4. Deistung A, Schweser F, Reichenbach JR. Overview of quantitative susceptibility mapping. *NMR in Biomedicine*. 2017;30(4). doi:10.1002/nbm.3569

5. Fukunaga M, Li TQ, Van Gelderen P, et al. Layer-specific variation of iron content in cerebral cortex as a source of MRI contrast. *Proceedings of the National Academy of Sciences of the United States of America*. 2010;107(8):3834-3839. doi:10.1073/pnas.0911177107

6. Stüber C, Morawski M, Schäfer A, et al. Myelin and iron concentration in the human brain: A quantitative study of MRI contrast. *NeuroImage*. 2014;93(P1):95-106. doi:10.1016/j.neuroimage.2014.02.026

7. Barbosa JHO, Santos AC, Tumas V, et al. Quantifying brain iron deposition in patients with Parkinson's disease using quantitative susceptibility mapping, R2 and R2*. *Magnetic Resonance Imaging*. 2015;33(5):559-565. doi:10.1016/j.mri.2015.02.021

8. Ulla M, Bonny JM, Ouchchane L, Rieu I, Claise B, Durif F. Is R2* a New MRI Biomarker for the Progression of Parkinson's Disease? A Longitudinal Follow-Up. *PLoS ONE*. 2013;8(3). doi:10.1371/journal.pone.0057904

9. Langkammer C, Ropele S, Pirpamer L, Fazekas F, Schmidt R. MRI for iron mapping in Alzheimer's disease. *Neurodegenerative Diseases*. 2014;13(2-3):189-191. doi:10.1159/000353756

10. Khalil M, Enzinger C, Langkammer C, et al. Quantitative assessment of brain iron by R2* relaxometry in patients with clinically isolated syndrome and relapsing-remitting multiple sclerosis. *Multiple Sclerosis*. 2009;15(9):1048-1054. doi:10.1177/1352458509106609

11. Maclaren J, Armstrong BSR, Barrows RT, et al. Measurement and Correction of Microscopic Head Motion during Magnetic Resonance Imaging of the Brain. *PLoS ONE*. 2012;7(11). doi:10.1371/journal.pone.0048088

12. Sloots JJ, Froeling M, Biessels GJ, Zwanenburg JJM. Dynamic brain ADC variations over the cardiac cycle and their relation to tissue strain assessed with DENSE at high-field MRI. *Magnetic Resonance in Medicine*. 2022;88(1):266-279. doi:10.1002/mrm.29209

13. Adams AL, Viergever MA, Luijten PR, Zwanenburg JJM. Validating faster DENSE measurements of cardiac-induced brain tissue expansion as a potential tool for investigating cerebral microvascular pulsations. *NeuroImage*. 2020;208. doi:10.1016/j.neuroimage.2019.116466

14. Morgan AG, Thrippleton MJ, Wardlaw JM, Marshall I. 4D flow MRI for non-invasive measurement of blood flow in the brain: A systematic review. *Journal of Cerebral Blood Flow and Metabolism*. 2021;41(2):206-218. doi:10.1177/0271678X20952014

15. Schnell S, Wu C, Ansari SA. 4D MRI flow examinations in cerebral and extracerebral vessels. Ready for clinical routine? HHS Public Access. *Curr Opin Neurol*. 2016;29(4):419-428. doi:10.1097/WCO.0000000000000341.4D

16. Tao Y, Rilling G, Davies M, Marshall I. Carotid blood flow measurement accelerated by compressed sensing: Validation in healthy volunteers. *Magnetic Resonance Imaging*. 2013;31(9):1485-1491. doi:10.1016/j.mri.2013.05.009

17. Schuchardt F, Schroeder L, Anastasopoulos C, et al. In vivo analysis of physiological 3D blood flow of cerebral veins. *European Radiology*. 2015;25(8):2371-2380. doi:10.1007/s00330-014-3587-x

18. Chen L, Beckett A, Verma A, Feinberg DA. Dynamics of respiratory and cardiac CSF motion revealed with real-time simultaneous multi-slice EPI velocity phase contrast imaging. *NeuroImage*. 2015;122:281-287. doi:10.1016/j.neuroimage.2015.07.073

19. Hermes D, Wu H, Kerr AB, Wandell BA. Measuring brain beats: Cardiac-aligned fast functional magnetic resonance imaging signals. *Human Brain Mapping*. 2023;44(1):280-294. doi:10.1002/hbm.26128

20. Petridou N, Schäfer A, Gowland P, Bowtell R. Phase vs. magnitude information in functional magnetic resonance imaging time series: toward understanding the noise. *Magnetic Resonance Imaging*. 2009;27(8):1046-1057. doi:10.1016/j.mri.2009.02.006

21. Menon RS. Postacquisition suppression of large-vessel BOLD signals in high-resolution fMRI. *Magnetic Resonance in Medicine*. 2002;47(1):1-9. doi:10.1002/mrm.10041

22. Bianciardi M, Toschi N, Polimeni JR, et al. The pulsatility volume index: An indicator of cerebrovascular compliance based on fast magnetic resonance imaging of cardiac and respiratory pulsatility. *Philosophical Transactions of the Royal Society A: Mathematical, Physical and Engineering Sciences*. 2016;374(2067). doi:10.1098/rsta.2015.0184

23. Budrys T, Veikutis V, Lukosevicius S, Gleizniene R, Monastyreckiene E, Kulakiene I. Artifacts in magnetic resonance imaging: How it can really affect diagnostic image quality and confuse clinical diagnosis? *Journal of Vibroengineering*. 2018;20(2):1202-1213. doi:10.21595/jve.2018.19756

24. Dagli MS, Ingeholm JE, Haxby JV. Localization of cardiac-induced signal change in fMRI. *NeuroImage*. 1999;9(4):407-415. doi:10.1006/nimg.1998.0424

25. Brooks JCW, Faull OK, Pattinson KTS, Jenkinson M. Physiological noise in brainstem fMRI. *Frontiers in Human Neuroscience*. 2013;(OCT). doi:10.3389/fnhum.2013.00623

26. Beissner F. Functional MRI of the Brainstem: Common Problems and their Solutions. *Clinical Neuroradiology*. 2015;25:251-257. doi:10.1007/s00062-015-0404-0

27. van der Zwaag W, Jorge J, Butticaz D, Gruetter R. Physiological noise in human cerebellar fMRI. *Magnetic Resonance Materials in Physics, Biology and Medicine*. 2015;28(5):485-492. doi:10.1007/s10334-015-0483-6

28. Deckers RHR, van Gelderen P, Ries M, et al. An adaptive filter for suppression of cardiac and respiratory noise in MRI time series data. *NeuroImage*. 2006;33(4):1072-1081. doi:10.1016/j.neuroimage.2006.08.006

29. Xu B, Liu T, Spincemaille P, Prince M, Wang Y. Flow compensated quantitative susceptibility mapping for venous oxygenation imaging. *Magnetic Resonance in Medicine*. 2014;72(2):438-445. doi:10.1002/mrm.24937

30. Larson TC, Kelly WM, Ehman RL, Wehrli FW. Spatial misregistration of vascular flow during MR imaging of the CNS: Cause and clinical significance. *American Journal of Neuroradiology*. 1990;11(5):1041-1048.

31. Gelderen P van, Zwart JA de, Starewicz P, Hinks RS, Duyn JH. Real-Time Shimming to Compensate for Respiration- Induced B0 Fluctuations. *Magnetic Resonance in Medicine*. Published online 2007.

32. Wymer DT, Patel KP, Burke WF, Bhatia VK. Phase-contrast MRI: Physics, techniques, and clinical applications. *Radiographics*. 2020;40(1):122-140. doi:10.1148/rg.2020190039

33. Godenschweger F, Kägebein U, Stucht D, et al. Motion correction in MRI of the brain. *Physics in Medicine and Biology*. 2016;61(5):R32-R56. doi:10.1088/0031-9155/61/5/R32

34. Welch EB, Felmlee JP, Ehman RL, Manduca A. Motion correction using the k-space phase difference of orthogonal acquisitions. *Magnetic Resonance in Medicine*. 2002;48(1):147-156. doi:10.1002/mrm.10179

35. Borup DD, Elkins CJ, Eaton JK. Effects of motion on MRI signal decay from micron-scale particles. *Journal of Magnetic Resonance*. 2019;305:152-161. doi:10.1016/j.jmr.2019.06.014

36. Yang X, Sammet S, Schmalbrock P, Knopp MV. Postprocessing correction for distortions in T2 decay caused by quadratic cross-Slice B0 inhomogeneity. *Magnetic Resonance in Medicine*. 2010;63(5):1258-1268. doi:10.1002/mrm.22316

37. Glover GH, Li TQ, Ress D. Image-based method for retrospective correction of physiological motion effects in fMRI: RETROICOR. *Magnetic Resonance in Medicine*. 2000;44(1):162-167. doi:10.1002/1522-2594(200007)44:1<162::AID-MRM23>3.0.CO;2-E

38. Agrawal U, Brown EN, Lewis LD. Model-based physiological noise removal in fast fMRI. *NeuroImage*. 2020;205. doi:10.1016/j.neuroimage.2019.116231

39. Tijssen RHN, Jenkinson M, Brooks JCW, Jezzard P, Miller KL. Optimizing RetroICor and RetroKCor corrections for multi-shot 3D FMRI acquisitions. *NeuroImage*. 2014;84:394-405. doi:10.1016/j.neuroimage.2013.08.062

40. Hennig J. K-space sampling strategies. *European Radiology*. 1999;9(6):1020-1031. doi:10.1007/s003300050788

41. Seginer A, Schmidt R. Messing up to clean up: Semi-randomized frequency selective space-filling curves to suppress physiological signal fluctuations in MRI. *Magnetic Resonance in Medicine*. 2023;90(6):2275-2289. doi:10.1002/mrm.29790

42. Seginer A, Niry D, Furman-Haran E, Kolb H, Schmidt R. Reducing blood flow pulsation artifacts in 3D time-of-flight angiography by locally scrambling the order of the acquisition at 3 T and 7 T. *Magnetic Resonance in Medicine*. Published online 2024. doi:10.1002/mrm.30196

43. Zhao C, Shao X, Yan L, Wang DJJ. k-space weighted image average (KWIA) for ASL-based dynamic MR angiography and perfusion imaging. *Magnetic Resonance Imaging*. 2022;86:94-106. doi:10.1016/j.mri.2021.11.017

44. Krämer M, Jochimsen TH, Reichenbach JR. Functional magnetic resonance imaging using PROPELLER-EPI. *Magnetic Resonance in Medicine*. 2012;68(1):140-151. doi:10.1002/mrm.23220

45. Forbes KPN, Pipe JG, Bird CR, Heiserman JE. PROPELLER MRI: Clinical testing of a novel technique for quantification and compensation of head motion. *Journal of Magnetic Resonance Imaging*. 2001;14(3):215-222. doi:10.1002/jmri.1176

46. Pipe J. Improved in-plane motion correction for PROPELLER MRI. *Proc Intl Soc Magn Reson Med*. 2001;9:2001.

47. Lee D, Pollock S, Whelan B, Keall P, Kim T. Dynamic keyhole: A novel method to improve MR images in the presence of respiratory motion for real-time MRI. *Medical Physics*. 2014;41(7). doi:10.1118/1.4883882

48. Pipe JG. Motion correction with PROPELLER MRI: Application to head motion and free-breathing cardiac imaging. *Magnetic Resonance in Medicine*. 1999;42(5):963-969. doi:10.1002/(SICI)1522-2594(199911)42:5<963::AID-MRM17>3.0.CO;2-L

49. Raynaud Q, Di Domenicantonio G, Yerly J, Dardano T, van Heeswijk RB, Lutti A. A characterization of cardiac-induced noise in R2* maps of the brain. *Magnetic Resonance in Medicine*. 2024;91(1):237-251. doi:10.1002/mrm.29853

50. Skare S, Andersson JLR. On the effects of gating in diffusion imaging of the brain using single shot EPI. *Magnetic Resonance Imaging*. 2001;19(8):1125-1128. doi:10.1016/S0730-725X(01)00415-5

51. Nunes RG, Jezzard P, Clare S. Investigations on the efficiency of cardiac-gated methods for the acquisition of diffusion-weighted images. *Journal of Magnetic Resonance*. 2005;177(1):102-110. doi:10.1016/j.jmr.2005.07.005

52. Zhang WT, Mainero C, Kumar A, et al. Strategies for improving the detection of fMRI activation in trigeminal pathways with cardiac gating. *NeuroImage*. 2006;31(4):1506-1512. doi:10.1016/j.neuroimage.2006.02.033

53. Mainero C, Zhang WT, Kumar A, Rosen BR, Sorensen AG. Mapping the spinal and supraspinal pathways of dynamic mechanical allodynia in the human trigeminal system using cardiac-gated fMRI. *NeuroImage*. 2007;35(3):1201-1210. doi:10.1016/j.neuroimage.2007.01.024

54. Hu X, Le TH, Parrish T, Erhard P. Retrospective estimation and correction of physiological fluctuation in functional MRI. *Magnetic Resonance in Medicine*. 1995;34(2):201-212. doi:10.1002/mrm.1910340211

55. Prieto C, Doneva M, Usman M, et al. Highly efficient respiratory motion compensated free-breathing coronary MRA using golden-step Cartesian acquisition. *Journal of Magnetic Resonance Imaging*. 2015;41(3):738-746. doi:10.1002/jmri.24602

56. Gottwald LM, Peper ES, Zhang Q, et al. Pseudo-spiral sampling and compressed sensing reconstruction provides flexibility of temporal resolution in accelerated aortic 4D flow MRI: A comparison with k-t principal component analysis. *NMR in Biomedicine*. 2020;33(4). doi:10.1002/nbm.4255

57. Peper ES, Gottwald LM, Zhang Q, et al. Highly accelerated carotid 4D flow MRI using Pseudo-Spiral Cartesian acquisition and a Total Variation constrained Compressed Sensing reconstruction. *Journal of Cardiovascular Magnetic Resonance*. Published online 2019:IN PRESS.

58. Tijssen RHN, Okell TW, Miller KL. Real-time cardiac synchronization with fixed volume frame rate for reducing physiological instabilities in 3D FMRI. *NeuroImage*. 2011;57(4):1364-1375. doi:10.1016/j.neuroimage.2011.05.070

59. Griswold MA, Jakob PM, Heidemann RM, et al. Generalized Autocalibrating Partially Parallel Acquisitions (GRAPPA). *Magnetic Resonance in Medicine*. 2002;47(6):1202-1210. doi:10.1002/mrm.10171

60. Lutti A, Corbin N, Ashburner J, et al. Restoring statistical validity in group analyses of motion-corrupted MRI data. *Human Brain Mapping*. 2022;43(6):1973-1983. doi:10.1002/hbm.25767

61. Loued-Khenissi L, Trofimova O, Vollenweider P, et al. Signatures of life course socioeconomic conditions in brain anatomy. *Human Brain Mapping*. 2022;43(8):2582-2606. doi:10.1002/hbm.25807

62. Trofimova O, Latypova A, DiDomenicantonio G, et al. Topography of associations between cardiovascular risk factors and myelin loss in the ageing human brain. *Communications Biology*. 2023;6(1). doi:10.1038/s42003-023-04741-1

63. Mugler JP, Brookeman JR. Three-dimensional magnetization-prepared rapid gradient-echo imaging (3D MP RAGE). *Magnetic Resonance in Medicine*. 1990;15(1):152-157. doi:10.1002/mrm.1910150117

64. Papp D, Callaghan MF, Meyer H, Buckley C, Weiskopf N. Correction of inter-scan motion artifacts in quantitative R1 mapping by accounting for receive coil sensitivity effects. *Magnetic Resonance in Medicine*. 2016;76(5):1478-1485. doi:10.1002/mrm.26058

65. Pruessmann KP, Weiger M, Scheidegger MB, Boesiger P. SENSE: Sensitivity encoding for fast MRI. *Magnetic Resonance in Medicine*. 1999;42(5):952-962. doi:10.1002/(SICI)1522-2594(199911)42:5<952::AID-MRM16>3.0.CO;2-S

66. Weiskopf N, Callaghan MF, Josephs O, Lutti A, Mohammadi S. Estimating the apparent transverse relaxation time (R2*) from images with different contrasts (ESTATICS) reduces motion artifacts. *Frontiers in Neuroscience*. 2014;8(SEP). doi:10.3389/fnins.2014.00278

67. Bilgic B, Costagli M, Chan KS, et al. Recommended implementation of quantitative susceptibility mapping for clinical research in the brain: A consensus of the ISMRM electro-magnetic tissue properties study group. *Magnetic Resonance in Medicine*. 2024;91(5):1834-1862. doi:10.1002/mrm.30006

68. Dymerska B, Eckstein K, Bachrata B, et al. Phase unwrapping with a rapid opensource minimum spanning tree algorithm (ROMEO). *Magnetic Resonance in Medicine*. 2021;85(4):2294-2308. doi:10.1002/mrm.28563

69. Eckstein K, Dymerska B, Bachrata B, et al. Computationally Efficient Combination of Multi-channel Phase Data From Multi-echo Acquisitions (ASPIRE). *Magnetic Resonance in Medicine*. 2018;79(6):2996-3006. doi:10.1002/mrm.26963

70. Smith SM. Fast robust automated brain extraction. *Human Brain Mapping*. 2002;17(3):143-155. doi:10.1002/hbm.10062

71. Hu W, Liu H, Chen D, et al. Coil combination of multichannel single voxel magnetic resonance spectroscopy with repeatedly sampled in vivo data. *Molecules*. 2021;26(13). doi:10.3390/molecules26133896

72. Chan KS, Marques JP. SEPIA—Susceptibility mapping pipeline tool for phase images. *NeuroImage*. 2021;227. doi:10.1016/j.neuroimage.2020.117611

73. Wei H, Dibb R, Zhou Y, et al. Streaking artifact reduction for quantitative susceptibility mapping of sources with large dynamic range. *NMR in Biomedicine*. 2015;28(10):1294-1303. doi:10.1002/nbm.3383

74. Ashburner J, Friston KJ. Unified segmentation. *NeuroImage*. 2005;26(3):839-851. doi:10.1016/j.neuroimage.2005.02.018

75. Feng X, Deistung A, Reichenbach JR. Quantitative susceptibility mapping (QSM) and R2* in the human brain at 3 T: Evaluation of intra-scanner repeatability. *Zeitschrift fur Medizinische Physik*. 2018;28(1):36-48. doi:10.1016/j.zemedi.2017.05.003

76. Wen J, Cross AH, Yablonskiy DA. On the role of physiological fluctuations in quantitative gradient echo MRI: Implications for GEPCI, QSM, and SWI. *Magnetic Resonance in Medicine*. 2015;73(1):195-203. doi:10.1002/mrm.25114

77. Atkinson IC, Lu A, Thulborn KR. Characterization and correction of system delays and eddy currents for MR imaging with ultrashort echo-time and time-varying gradients. *Magnetic Resonance in Medicine*. 2009;62(2):532-537. doi:10.1002/mrm.22016

78. Aldefeld B, Börnert P. Effects of gradient anisotropy in MRI. *Magnetic Resonance in Medicine*. 1998;39(4):606-614. doi:10.1002/mrm.1910390414

79. Bieri O, Markl M, Scheffler K. Analysis and compensation of eddy currents in balanced SSFP. *Magnetic Resonance in Medicine*. 2005;54(1):129-137. doi:10.1002/mrm.20527

80. Jezzard P, Barnett AS, Pierpaoli C. Characterization of and correction for eddy current artifacts in echo planar diffusion imaging. *Magnetic Resonance in Medicine*. 1998;39(5):801-812. doi:10.1002/mrm.1910390518

81. Spees WM, Buhl N, Sun P, Ackerman JJH, Neil JJ, Garbow JR. Quantification and compensation of eddy-current-induced magnetic-field gradients. *Journal of Magnetic Resonance*. 2011;212(1):116-123. doi:10.1016/j.jmr.2011.06.016

82. Li J, Wang Y, Jiang Y, Xie H, Li G. Image correction during large and rapid B0 variations in an open MRI system with permanent magnets using navigator echoes and phase compensation. *Magnetic Resonance Imaging*. 2009;27(7):988-993. doi:10.1016/j.mri.2009.01.022

83. Lustig M, Donoho D, Pauly JM. Sparse MRI: The application of compressed sensing for rapid MR imaging. *Magnetic Resonance in Medicine*. 2007;58(6):1182-1195. doi:10.1002/mrm.21391

84. Bustin A, Lima da Cruz G, Jaubert O, Lopez K, Botnar RM, Prieto C. High-dimensionality undersampled patch-based reconstruction (HD-PROST) for accelerated multi-contrast MRI. *Magnetic Resonance in Medicine*. 2019;81(6):3705-3719. doi:10.1002/mrm.27694

85. Chiew M, Smith SM, Koopmans PJ, Graedel NN, Blumensath T, Miller KL. K-t FASTER: Acceleration of functional MRI data acquisition using low rank constraints. *Magnetic Resonance in Medicine*. 2015;74(2):353-364. doi:10.1002/mrm.25395

86. Bert RJ, Settipalle N, Muddasani D, et al. ECG Gating Is More Precise Than Peripheral Pulse Gating When Quantifying Spinal CSF Pulsations Using Phase Contrast Cine MRI. *Academic Radiology*. 2020;27(4):552-562. doi:10.1016/j.acra.2019.06.015

9. Supplementary material

9.1. Analysis of the cardiac-triggered sampling

Further analyses were performed to investigate why cardiac-triggered sampling did not reduce the variability of the R_2*/QSM estimates across repetitions. First, an examination of the finger pulse-oximeter data was conducted, to verify that cardiac-triggering was performed as expected.

9.1.1. Examination of the pulse-oximeter data

The pulse-oximeter signals recorded at the participants' finger were saved after acquisition of the MRI data. Visual inspection of each pulse-oximeter data was performed. The signal was clean and the peaks of the pulse wave seemed to have been accurately detected. Figure S1A shows a typical time-course of pulse-oximeter signal, with the corresponding periods of data acquisition and suspension. Data acquisition was stopped when reaching the cardiac-triggering lines, only to be restarted when reaching detecting the next peak of the pulse wave. The peak of the pulse wave detection was conducted in real time by the MR sequence, from the detection of a local maximum in the pulse-oximeter signal with an amplitude above 2500 (the mean value of the pulse-oximeter signal). Even if simplistic, this method gives very accurate results and does not trigger on the second peak that happen during the diastole, after the dicrotic notch.

Combining the pulse-oximeter data with the k-space trajectory allows examination of the cardiac phase at the time of acquisition of each k-space data point (Figure S1B). Along the fast phase-encode direction, the time span between consecutive points (TR=40ms) is small compared to the cardiac period and the cardiac phase varies smoothly. For a standard linear trajectory (left), the phase of the cardiac cycle shows abrupt changes along the slow phase-encode direction. As expected with cardiac-triggering (right), the phase of the cardiac cycle is 0 (peak of the pulse wave detection) at the cardiac-triggering lines. As a result of the cardiac-triggering lines, the phase of the cardiac cycle is highly consistent along the slow encoding direction, at the centre of k-space. At the centre of k-space, the phase of the cardiac cycle shows little variability across repetitions and participants (Figure S1C).

According to these analyses, the cardiac triggering seems to have worked as expected. The peaks of the pulse wave were accurately detected and the centre of k-space is acquired in the first quarter of the cardiac cycle, which is the least noisy part of the cardiac-cycle. The poor performance of the cardiac-triggering sampling doesn't seem to originate from an implementation problem.

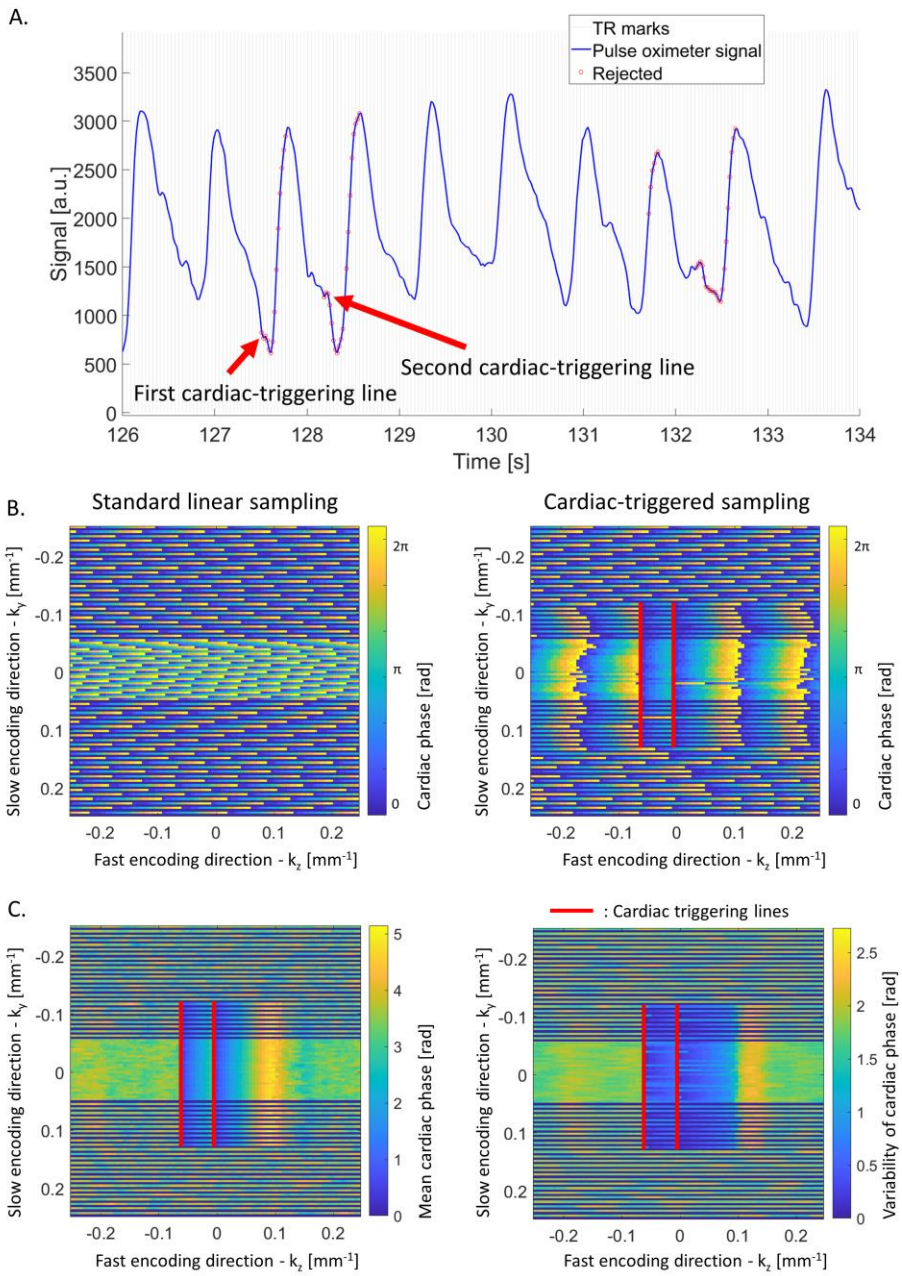

Figure S1: Analysis of the performance of cardiac triggering. (A) Representative example of pulse oximeter signal (blue plot). The grey vertical lines show consecutive blocks of multi-echo readouts (TR). The first and second triggering lines are indicated with arrows, and the time points where data acquisition was suspended are highlighted with red circles. (B) Example distribution of the phase of the cardiac cycle during the acquisition of the k-space data. Along the fast phase-encode direction, the time span between consecutive points (TR=40ms) is small compared to the cardiac period and the cardiac phase varies smoothly. For a standard linear trajectory (left), the phase of the cardiac cycle shows abrupt changes along the slow phase-encode direction. For the cardiac-triggered sampling (right), the cardiac phase is near 0 at the k-space centre and is highly consistent due to the cardiac-triggering lines (red). The data were acquired with a GRAPPA acceleration factor of 2 with 24 reference lines at the k-space centre. The missing lines are shown in dark blue. (C) Mean (left) and variability (right) of the acquired cardiac phase across repetitions and participants using the cardiac-triggered sampling.